

Electron-donating Effect of Hydantoin Derivative Inhibitor on the Enhanced Anticorrosion Capacity for Mild Steel in Hydrochloric Acid Medium

Junjie Zhu ¹, Hua Hao ^{2,*}, Xingwen Zheng ³

¹ College of Chemistry and Materials Engineering, Beijing Technology and Business University, Beijing 100048, China;

² Institute of Chemistry, Chinese Academy of Sciences, Beijing 100190, China;

³ Key Laboratory of Material Corrosion and Protection of Sichuan Province, Sichuan University of Science & Engineering, Zigong 643000, China

*E-mail: haohuaiccas@126.com

Received: 5 November 2021 / Accepted: 22 December 2021 / Published: 2 February 2022

Hydantoin (HDT) and its derivative (allantoin, ALT) were evaluated as corrosion inhibitors for 20# steel in 1 M HCl solution at 303 K through gravimetric test, potentiodynamic polarization, electrochemical impedance spectroscopy and surface analysis. Especially, the electron-donating effect of extra acid diamide group (ALT) on improving the anticorrosion efficiency was observed: the inhibition efficiency of ALT-inhibited specimen (maximum of 96.12%) was higher than the counterpart protected by HDT at the same dosage. Electrochemical results showed that the corrosion current density was largely suppressed along with the elevated interfacial charge transfer resistance for steel in HCl solution with ALT. Due to the effective adsorption, both HDT- and ALT-inhibited specimens emerged the inferior surface wettability as compared to that of blank control; surface morphology also evidenced the better protection of ALT than that of HDT. Theoretical modelling indicated that acid diamide group on ALT intensified the negative potential of hydantoin ring, which played a pivotal role in chemisorption and the ensuing corrosion inhibition mechanism for 20# steel in HCl solution.

Keywords: hydantoin; corrosion inhibitor; electrochemical evaluation; density functional theory; molecular dynamics simulation

1. INTRODUCTION

Corrosion phenomenon prevalently exists in metallic facilities that severely hazards industrial infrastructures in both safety and economy aspects [1-3]. Therefore, the effective anticorrosion strategy attracts intense research interests, and tremendous efforts have been devoted to alleviating the negative impact of metal degradation [4-6]. Consequently, structural optimization, electrochemical protection,

applying coatings and corrosion inhibitors consist of the main routes to retard metal corrosion in various aggressive media [7-9]. Thereinto, employing corrosion inhibitors is deemed as one of the most fascinating way to mitigate metal degradation due to the significant advantages of facile operation, low cost and high efficiency, and has garnered great interest in scientific and industrial communities [10]. For instance, acidic pickling should be periodically performed for industrial equipment and pipelines to remove the deposited scale and rust. Therein, corrosive mineral acids, such as HCl and H₂SO₄, are frequently utilized as the cleaning solutions, which inevitably cause the electrochemical corrosion of the underneath metals [11]. Whereupon, corrosion inhibitors must be involved in the pickling media to inhibit the unnecessary damage for metal substrates.

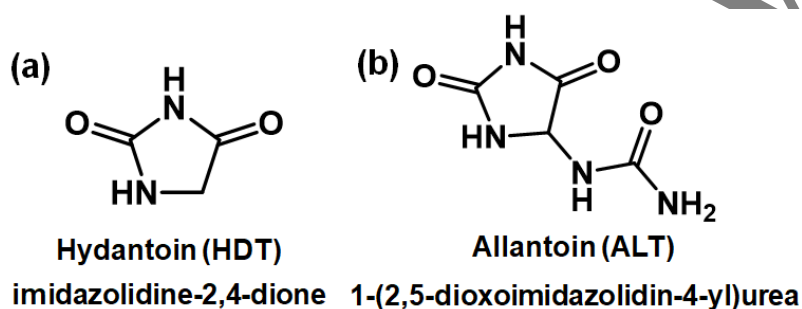
Compared with inorganic counterparts (e.g., chromate, nitrite and phosphate), organic corrosion inhibitors earn the salient characteristics such as low toxicity, eco-friendly and biocompatibility [12-14]. As is well acknowledged, the heteroatoms, unsaturated bonds and conjugated system of organic inhibitors may donate the unpaired electrons toward unoccupied d-orbit of metal atoms (e.g., iron), and thus occur chemisorption on the substrate [8, 15]. Recently, Olasunkanmi et al. [16] employed two propanone derivatives of quinoxalin-6-yl-4,5-dihydropyrazole as corrosion inhibitors for mild steel in 1 M HCl solution. They found that two derivatives behaved as the mixed-type inhibitor assembled on steel surface with a maximum protection efficiency of 93.69%. Gaber et al. [17] used 2-cyano-N-(4-morpholinobenzylidene) acetohydrazide for mitigating the corrosion of 304 stainless steel in 1 M H₂SO₄ solution. The adsorption of this inhibitor followed by Langmuir model, which emerged promising anticorrosion effect for stainless steel in the aggressive medium. Huang and co-workers [18] evaluated the corrosion inhibition efficiency of procyanidin B2 (PCB2) for Q235 steel in 1 M HCl solution through electrochemical and gravimetric approaches. The results showed that PCB2 exhibited favorable protection efficiency acting as a mixed-type corrosion inhibitor along with the satisfactory antibacterial activity. As per the reports of different literatures, many compounds with the similar chemical structure exhibit the analogous inhibitory power for metals in aggressive media [19]. However, the specific role of structural differences among homologous inhibitors in the anticorrosion efficiency has been scarcely studied.

On that account, hydantoin (HDT) and its derivative (allantoin, ALT) were used as potential corrosion inhibitor for 20# steel in 1 M HCl solution. Multiple heteroatoms and unsaturated bonds in HDT and ALT endow them viable for the anticorrosive application, in which ALT owned the extra acid diamide group with electron-donating effect. The corrosion inhibition efficiencies of HDT and ALT were estimated by gravimetric tests, electrochemical and surface analyses. The electron-donating effect of acid diamide group was revealed by density functional theory (DFT) calculations in dominant solvent models; and the adsorption mechanism of HDT and ALT was disclosed by molecular dynamics (MD) simulations. Ultimately, the enhanced anticorrosion effect of ALT was illustrated through experimental and theoretical evidences. This study may pave an avenue for exploring the electronic effect of key substituents on the integral anticorrosion efficacy of corrosion inhibitors.

2. EXPERIMENTAL SECTION

2.1 Materials and solutions

All reagents used herein were of analytical pure. HDT and ALT were supplied by Beijing Innochem Co., LTD (China) and their structures are shown in Scheme 1. Concentrated HCl solution (37 wt%) and anhydrous ethanol were obtained from Beijing Chemical Works (China). The HCl stock solution was diluted to 1 M by lab-made deionized water as the corrosive medium. 20# steel standard coupons with a dimension of $50 \times 25 \times 2 \text{ mm}^3$ were utilized as the substrates (Wuhan Research Institute of Materials Protection, China). Before utilization, all coupons were degreased by ethanol, successively polished with SiC paper from 200 to 2000 mesh, ultrasonicated in ethanol bath, dried under nitrogen current, accurately weighed and kept in a silica gel-sealed desiccator.



Scheme 1 Molecular structures of (a) hydantoin (HDT) and (b) allantoin (ALT)

2.2 Gravimetric test

Triplicate polished specimens were mounted on an RCC-III rotation corrosion instrument (Qinyou Company, China), which were immersed in 1 M HCl solution without and with various concentrations of HDT or ALT at the pre-set temperature under 72 r/min. After 24 h immersion, the specimens were withdrawn, alternately cleaned by deionized water and ethanol, dried and re-weighed. According to the given formulae, the corrosion rate (v , mm/a) and corresponding inhibition efficiency (IE_w , %) were calculated [20]:

$$v = \frac{\Delta m \cdot 8.76}{S \cdot t} \quad (1)$$

$$IE_w = \frac{v_0 - v_t}{v_0} \times 100\% \quad (2)$$

where Δm denotes the mass loss of steel before and after immersion; S denotes the surface area of the specimen; t denotes the immersion period; v_0 and v_t denote the corrosion rates of uninhibited and inhibited specimens, respectively.

2.3 Electrochemical evaluation

All electrochemical measurements were fulfilled via a PGSTAT 302N workstation (Metrohm, Switzerland) in a three-electrode cell at 303 K, in which 20# steel sealed by epoxy resin (exposure area: 1 cm²), Ag/AgCl_{sat} and Pt mesh were assembled as working, reference and counter electrodes, respectively. The working electrodes were polished with the same protocol as the abovementioned procedure. Before each assay, working electrodes were conditioned in the corrosive solution for at least 30 min to stabilize the open circuit potential (E_{ocp}). Potentiodynamic polarization was conducted in a potential range of -250 – 250 mV vs. E_{ocp} with a scan rate of 1 mV/s. According to the derived corrosion current density (i_{corr}), the inhibition efficiency (IE_p) was obtained using the equation:

$$IE_p = \frac{i_{corr}^0 - i_{corr}^i}{i_{corr}^0} \times 100\% \quad (3)$$

where i_{corr}^0 and i_{corr}^i are the corrosion current densities of steel electrodes in HCl solution without and with various concentrations of inhibitor. Electrochemical impedance spectra (EIS) registered at E_{ocp} were performed in a frequency range from 10⁵ – 10⁻¹ Hz. Based on the value of charge transfer resistance (R_{ct}), the inhibition efficiency (IE_z) was calculated:

$$IE_z = \frac{R_{ct}^i - R_{ct}^0}{R_{ct}^i} \times 100\% \quad (4)$$

where R_{ct}^0 and R_{ct}^i are the charge transfer resistances of steel electrodes in HCl solution without and with various concentrations of inhibitor.

2.4 Surface analysis

A DSX 1000 digital microscope (OLYMPUS, Japan) was exploited to capture the macroscopic appearances of steel specimens before and after 24 h immersion in 1 M HCl solution without and with the optimal concentration of HDT or ALT at 303 K. Furthermore, the same specimens were incised into 1×1 cm², and detected by a QUANTA FEG 250 scanning electron microscope (SEM, FEI, USA). The surface wettability of different specimens was checked through an OCA 35 contact angle goniometer (Dataphysics, Germany).

2.5 Theoretical simulation

The specific chemical states of HDT and ALT in 1 M HCl solution were initially ascertained by MarvinSketch software for the subsequent electronic and atomic scale calculations completed with Materials Studio (BIOVIA, France). First-principles calculations based on DFT were conducted with the implanted DMol3 code. Dominant solvent models for inhibitors were built as the previous reports [9, 11, 12]. The reactive parameters, namely optimized configuration, highest occupied molecular orbit (HOMO), lowest unoccupied molecular orbital (LUMO) and electrostatic potential (ESP) mapping, were calculated using Generalized Gradient Approximation of Perdew–Burke–Ernzerhof exchange correlation. The d-polarization functions were utilized as the basis set.

The adsorption of HDT and ALT on steel surface was also modeled by molecular dynamics (MD) simulation using Forcite module. Fe (100) plane was chosen as the target surface, which was cleaved

with five layers accompanied by a vacuum slab of 20 Å. A periodic box with a dimension of 22.76×22.76×31.74 Å³ was built for the adsorption of HDT or ALT, in which Fe atoms were frozen to preclude the crystal change. Referring to the actual HCl solution, 330 H₂O, 5 H₃O⁺, 5 Cl⁻ ions and one inhibitor were involved in the box, which was fully optimized to the ground state. Dynamic task was carried out under canonical NVT ensemble at 303 K for 1000 ps with 1 fs step. The interaction energy (E_{inter} , kJ/mol) between inhibitor and Fe (100) plane was acquired by the following expression:

$$E_{\text{inter}} = E_{\text{total}} - (E_{\text{Fe+sol}} + E_{\text{inh}}) \quad (5)$$

where E_{total} , $E_{\text{Fe+sol}}$ and E_{inh} are the energies of whole system, ion surface with solution and single inhibitor, respectively.

3. RESULTS AND DISCUSSION

3.1 Gravimetric tests and the derived adsorption thermodynamics and corrosion kinetics

The corrosion inhibition effects of HDT and ALT for 20# steel in 1 M HCl solution were preliminary evaluated by gravimetric method for 24 h at pre-set temperatures. Figure 1 presents v and the corresponding IE_w variations for steel in HCl solution without and with different concentrations of HDT and ALT. As shown in Figure 1a, v persistently decreases upon the addition of both inhibitors at each temperature, indicating that steel deterioration is mitigated in the presence of HDT or ALT. Accordingly, IE_w in Figure 1b monotonously increases with the augment of inhibitor concentration under a constant temperature. The alleviated corrosion of steel in HCl solution depends strongly on the effective adsorption of studied compounds, which forms a barrier layer at the steel/electrolyte interface isolating the underneath metal from the attack of corrosive species (e.g., Cl⁻) in the ambient environment [21]. Increasing temperature partially impairs the corrosion inhibition effect of HDT and ALT for the aggravated v and the ensuing decline of IE_w . High medium temperature inevitably accelerates the particle motion and elevates interfacial disorder, impeding the initial recognition and the subsequent adsorption of inhibitor molecules on steel surface [22]. Hence, the inhibitory effects of both compounds are weakened by increasing the ambient temperature. Additional insight into the variations of v and IE_w features that the anticorrosive efficacy of ALT is superior over that of HDT counterpart with the same concentration owing to the more obvious suppressing on v at each temperature. Remarkably, the maximum IE_w for ALT achieves as 96.12% with 1.0 mM dosage at 303 K, which is higher than that associated with HDT (89.13%). From the standpoint of structure-activity relationship, the difference in chemical structure between HDT and ALT may be responsible for the varied protection effect (discussed *vide infra*).

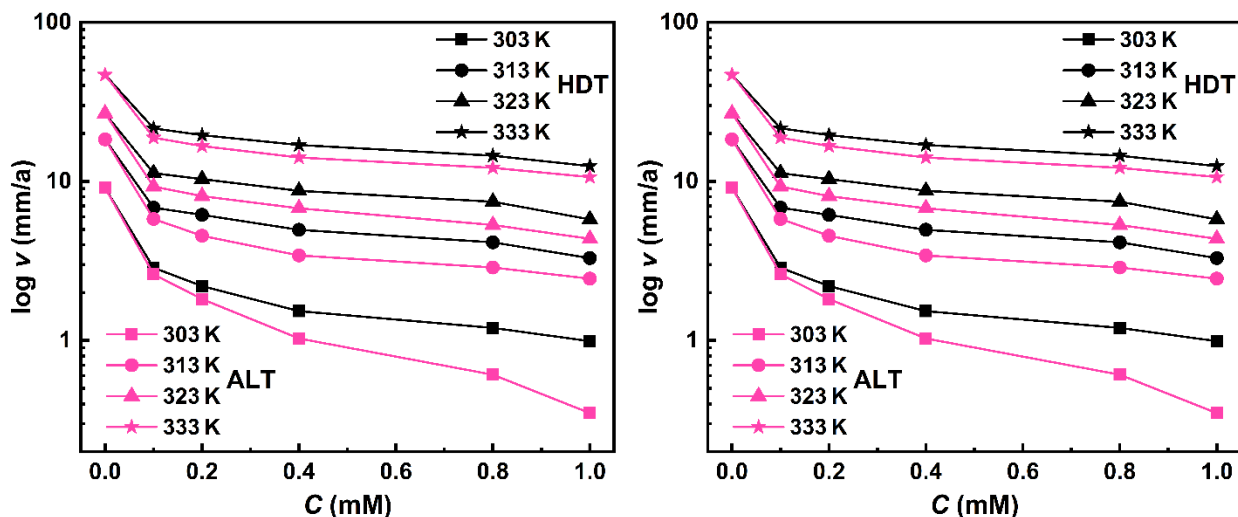


Figure 1. Corrosion rates (a) and the corresponding inhibition efficiencies (b) for 20# steel in 1 M HCl solution with different concentrations of HDT and ALT at allocated temperatures

The adsorption nature of corrosion inhibitor on metal surface can be described by various isotherms [7, 23, 24]. Deriving from gravimetric findings, IE_w and the resulting surface coverage (θ) by adsorbed inhibitor were utilized to attempt different isotherms. Thereinto, Langmuir isotherm yields the best outcomes (Figure 2), which can be expressed as follows [25]:

$$\theta = IE_w/100 \tag{6}$$

$$\frac{c}{\theta} = C + \frac{1}{K_{ads}} \tag{7}$$

$$K_{ads} = \frac{\exp(-\Delta G_{ads}/RT)}{55.5} \tag{8}$$

where C denotes the concentration of inhibitor; K_{ads} denotes the equilibrium constant that determines the adsorption strength and the ultimate protection capacity of corrosion inhibitor; ΔG_{ads} denotes Gibbs free energy for the adsorption process; 55.5 is the molar concentration of water; R and T denote gas constant and Kelvin temperature, respectively. High regression coefficients (R^2) in Figure 2 signify the favorable linearity, and thus the feasibility of Langmuir model. Moreover, the slope of each plot closes to unity, revealing that a monolayer is formed on steel surface for HDT and ALT with negligible intermolecular interactions [3].

The fitted K_{ads} and ΔG_{ads} for adsorbed inhibitors on 20# steel surface in 1 M HCl solution at different temperatures are compiled in Table 1. Large magnitude of K_{ads} reveal the potent adsorption of HDT and ALT on steel surface in HCl solution. However, K_{ads} decreases with the augment of temperature for each compound, which features the partial desorption of inhibitor molecules from the steel substrate. Negative sign of ΔG_{ads} in Table 1 evidences the spontaneous adsorption of HDT and ALT on steel surface [25]. As is known, ΔG_{ads} around -20 kJ/mol or more positive indicates the physisorption including electrostatic attraction; while, that less than -40 kJ/mol corresponds to the chemisorption resulting from the electrons transfer between the inhibitor and metal surface [26-28]. All ΔG_{ads} values in Table 1 extremely close to -40 kJ/mol, implying that physicochemical adsorption nature dominates their corrosion inhibition mechanism for steel in HCl medium. Noteworthily, K_{ads} and ΔG_{ads}

values associated with ALT are generally superior as compared to those of HDT under the same temperature. This is credited to the stronger and denser ALT layer formed at the steel/electrolyte interface than HDT counterpart.

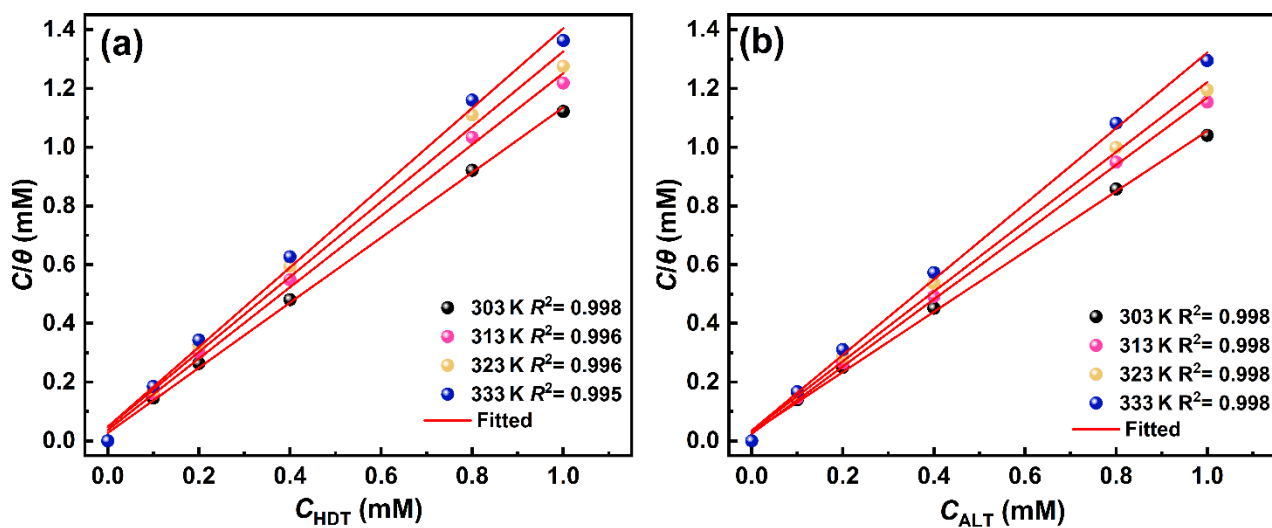


Figure 2. Langmuir models for the adsorption of HDT (a) and ALT (b) on 20# steel in 1 M HCl solution at allocated temperatures

Table 1. Thermodynamic parameters for HDT and ALT adsorbed on steel surface

Species	Temperature (K)	$K_{\text{ads}} (\times 10^3, \text{L/mol})$	$\Delta G_{\text{ads}} (\text{kJ/mol})$
HDT	303	34.1	-36.6
	313	27.0	-37.0
	323	21.4	-37.5
	333	20.8	-38.6
ALT	303	34.5	-36.4
	313	41.0	-38.1
	323	30.0	-38.5
	333	28.0	-39.5

To clarify the corrosion kinetics of 20# steel in 1 M HCl solution without and with different inhibitor concentrations, Arrhenius and transition state equations were deployed with the following relationship [11, 23]:

$$\ln v = \ln A - \frac{E_a}{RT} \quad (9)$$

$$\ln \frac{v}{T} = \ln \frac{R}{Nh} + \frac{\Delta S_a}{R} - \frac{\Delta H_a}{RT} \quad (10)$$

where v , R and T have the same meanings as the aforementioned definitions; besides, A denotes Arrhenius frequency factor; N denotes the molar constant; E_a denotes the corrosion activation energy; ΔH_a and ΔS_a denote the activation enthalpy and entropy, respectively. Figure 3 depicts Arrhenius and

transition state plots for steel in HCl solution without and with various concentrations of HDT and ALT at allocated temperatures. As per the slope and intercept of each curve in Figure 3, the corrosion kinetic parameters were fitted and are recorded in Table 2. Clearly, E_a gradually increases as the concentration of HDT or ALT increases, suggesting the elevated barrier for electrochemical corrosion due to the adsorption of more inhibitor molecules [5].

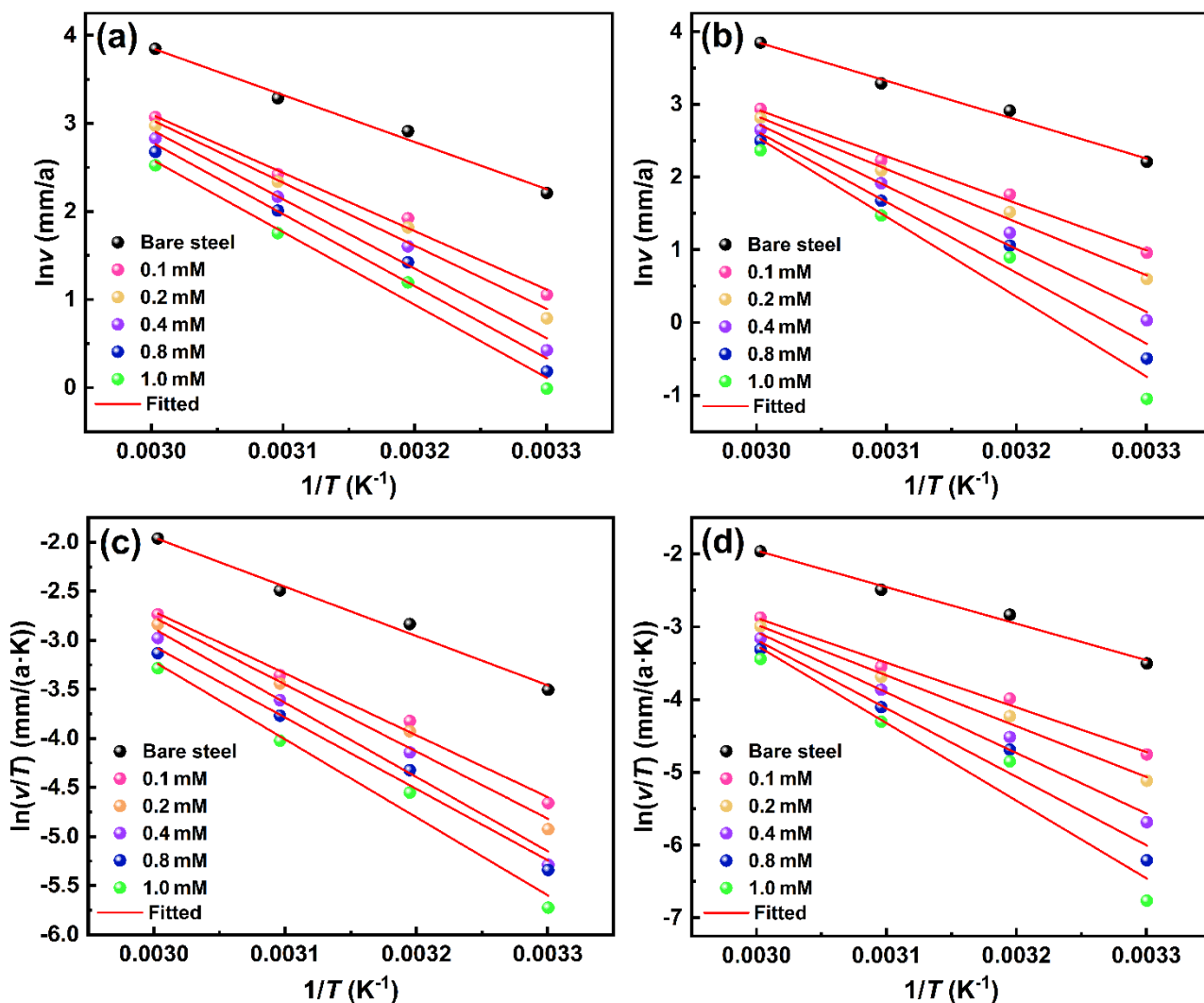


Figure 3. Arrhenius (a, b) and transition state (c, d) plots for 20# steel in 1 M HCl solution without and with different concentrations of HDT (left) or ALT (right)

Positive ΔH_a values coincide well with the endothermic essence of metal dissolution in HCl medium [29]. Besides, ascending ΔH_a with the increase in inhibitor concentration indicates their anticorrosive capacity for steel specimens in HCl solution since the occurrence of corrosion requires more latent heat in the presence of inhibitor [14]. Notably, all E_a values are larger than their ΔH_a analogs, disclosing that proton gaseous reduction is involved in the electrochemical corrosion [15]. Negative ΔS_a values feature the decreased disorder at steel/electrolyte interface, in which the formation and association

of activated complex, rather than dissociation, are the determining-step of system velocity [30]. Comparing kinetic parameters for HDT-inhibited system with those for ALT-inhibited counterpart supports that ALT exerts more pronounced protection capacity than HDT. In detail, higher ΔH_a for ALT-inhibited system articulates the more degrading difficulty of steel in HCl solution than the system with HDT. Meanwhile, less negative ΔS_a values for the steel protected by ALT also reveal that more ALT molecules are assembled on steel surface, and thereby provide enhanced anticorrosion efficacy.

Table 2. Corrosion kinetic parameters for 20# steel in 1 M HCl solution without and with different concentrations of HDT or ALT

Species	Concentration (mM)	E_a (kJ/mol)	ΔH_a (kJ/(mol·K))	ΔS_a (J/(mol·K))
Blank	0	44.4	41.7	-88.5
HDT	0.1	54.9	52.4	-62.9
	0.2	59.5	56.8	-50.0
	0.4	65.5	62.8	-32.9
	0.8	67.9	60.4	-41.6
	1.0	68.6	66.0	-26.2
ALT	0.1	55.7	51.0	-68.2
	0.2	60.6	58.0	-48.1
	0.4	71.8	69.2	-15.4
	0.8	80.8	78.2	-10.7
	1.0	91.3	88.6	-1.4

3.2 Surface analysis

Figure 4 illustrates the macroscopic and microscopic morphologies of steel specimens before and after 24 h immersion in 1 M HCl solution without and with 1 mM HDT or ALT at 303 K. Besides, the contact angles (inset of Figure 4) of different samples are also presented to document the occurrence of inhibitor adsorption pending the immersion period. A clean and smooth surface is observed for newly polished sample in Figure 4a and e, which owns the hydrophilic property with a contact angle of 40.89° . On the contrary, a rusty appearance is found in Figure 4b for the uninhibited specimen. Accordingly, seriously damaged morphology with plenty of pits and cracks is seen in Figure 4f, which results from the aggressive attack of H_3O^+ and Cl^- during immersion. The contact angle of this sample lowers to 18.63° due to capillary effect caused by corrosion pits [31, 32]. Fortunately, the presence of HDT and ALT in HCl solution provides the relatively flat surfaces without obvious corrosion signs as shown in Figure 4c and d, respectively. Consequently, smoother surface morphologies are displayed in Figure 4g and h. Further comparing Figure 4g with Figure 4h documents that the steel surface protected by ALT is more intact than the HDT-inhibited analogue. As expected, larger contact angle is acquired for the steel specimen after immersion in ALT-containing solution (82.83°) than that for the sample immersed with HDT (66.34°).

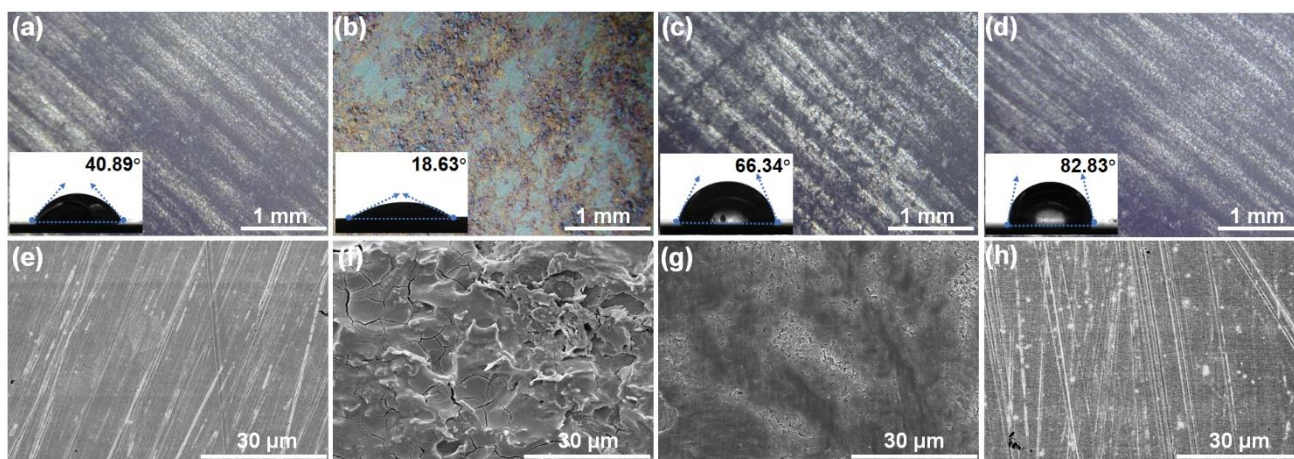


Figure 4. Optical (upper, inset: contact angles) and SEM images for 20# steel after 24 h immersion in 1 M HCl solution: freshly polished (a, e), without (b, f) and with 1 mM HDT (c, g), ALT (d, h) at 303 K

3.3 Electrochemical measurement

3.3.1 Electrochemical thermodynamics and kinetics

E_{ocp} evolution with time can be deemed as an implication for corrosion thermodynamic tendency of metals in aggressive solutions [12]. The variations of E_{ocp} for 20# steel in 1 M HCl solution with different concentrations of HDT and ALT at 303 K are shown in Figure 5a and c, respectively. As is seen, all the curves earn the pseudo-equilibrium at the end of exposure period, portending the established stability of steel electrode in HCl solution. It is noted that E_{ocp} shifts to nobler direction in the presence and with the increasing concentration of both compounds. The elevated E_{ocp} signifies the improved thermodynamic barrier against metal dissolution in corrosive media [4]. Hence, HDT and ALT hinder the electrochemical corrosion of 20# steel in HCl medium, especially at higher dosage.

Figure 5b and d displays the polarization curves for 20# steel in 1 M HCl solution with different concentrations of HDT and ALT at 303 K, respectively. For HDT-inhibited system given in Figure 5b, both anodic and cathodic branches are suppressed on the addition of HDT, revealing that steel dissolution and hydrogen evolution at the steel/solution interface are simultaneously inhibited due to the adsorption of HDT [8]. By increasing HDT concentration in the corrosive medium, the gradually compact layer is formed on steel surface, resulting in the further downward shift of polarization curve. Similar inhibition behavior is observed in Figure 5d for the steel immersed in HCl solution in the presence of ALT. Notably, the suppression degree for ALT-inhibited specimen is more salient than that of HDT-inhibited analogue with the same concentration. This discloses the superior anticorrosion effect of ALT as compared to that of HDT.

To quantitatively compare the corrosion mitigation efficiency of HDT and ALT for 20# steel in HCl solution, Tafel extrapolation was performed on polarization curves to obtain electrochemical kinetic parameters, namely corrosion potential (E_{corr}), i_{corr} , anodic (β_a) and cathodic (β_c) slopes, which are tabulated in Table 3. It is clear in this table that E_{corr} becomes more positive as the concentration of inhibitor increases.

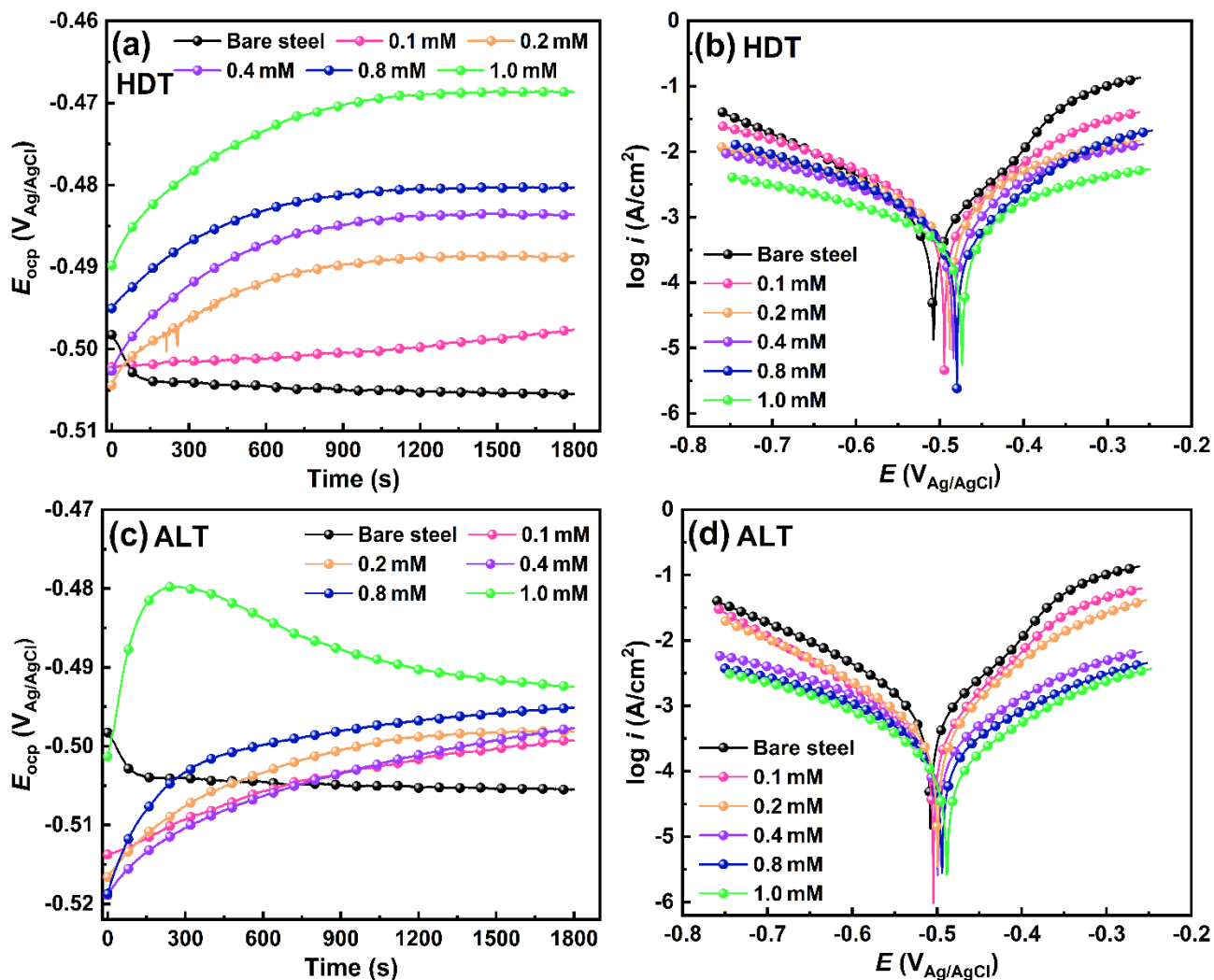


Figure 5. Evolution of E_{ocp} with time (a, c) and polarization curves (b, d) for 20# steel in 1 M HCl solution with different concentrations of HDT (upper) and ALT (lower) at 303 K

Table 3. Kinetic parameters for 20# steel in 1 M HCl solution with different concentrations of HDT and ALT at 303 K

Species	C_{inh} (mM)	$-E_{corr}$ (mV)	i_{corr} (mA/cm ²)	β_a (mV/dec)	$-\beta_c$ (mV/dec)	IE _p (%)
Blank	0	508	11.38	96	86	/
HDT	0.1	496	3.37	105	97	70.39
	0.2	488	2.25	123	105	80.23
	0.4	484	1.54	126	106	86.47
	0.8	480	1.20	119.	101	89.46
	1.0	473	0.98	132	119	91.39
ALT	0.1	504	3.10	98.	84	72.76
	0.2	499	1.73	98	84	84.80
	0.4	499	1.12	107	101	90.16
	0.8	494	0.57	109	104	94.99
	1.0	489	0.55	111	108	95.17

Coupling with the simultaneous inhibition of anodic and cathodic plots depicted in Figure 5b and d, HDT and ALT can be deemed as the mixed-type corrosion inhibitors with dominant anodic effect [33]. This inference is also supported by the remarkable increase in β_a as compared to the variation of β_c for both compounds. In the case of HDT-inhibited specimens, i_{corr} decreases from 11.38 mA/cm² (blank) to 0.98 mA/cm² (1 mM HDT) yielding the maximum IE_p of 91.39%. In contrast, i_{corr} value for the specimen in the presence of optimal ALT concentration further decreases to 0.55 mA/cm² with an IE_p of 95.17%.

3.3.2 EIS

EIS provides deep clarification of corrosion retardation mechanism for inhibitors in a non-destructive manner [34]. Nyquist and Bode spectra for 20# steel in 1 M HCl solution with various concentrations of HDT and ALT at 303 K are summarized in Figure 6. Nyquist plots given in Figure 6a and c show the same shape of suppressed semi-circle, which is attributed to the surface heterogeneity and micro-roughness of solid electrode [6]. Moreover, similar shape of these curves with a single capacitive loop indicates the unaffected corrosion mechanism of steel in the inhibited solution that is mainly controlled by interfacial charge transfer [35]. The diameter of capacitive circle in Figure 6a and c enlarges on the addition of HDT and ALT, which gets enhanced with the increasing inhibitor concentration. This reveals the concentration-dependent corrosion inhibition for both compounds toward steel specimen in HCl solution, for which the charge transfer at steel/electrolyte interface is effectively dampened [36]. The dulled interfacial charge transfer is also evidenced by Bode plots shown in Figure 6b and d. The variations of Bode modulus for HDT and ALT indicate that low-frequency resistance ($|Z_{0.1\text{Hz}}|$) is progressively elevated as both inhibitor concentrations increase. In addition, the Bode phase angle gradually increases with the broadened width for HDT- and ALT-inhibited systems, which implies the intensified interfacial capacitance due to inhibitor adsorption [37].

Randles equivalent circuit (inset of Figure 6c) was utilized to fit the acquired impedance data, in which constant phase element (CPE) was introduced instead of pure capacitance to compensate the dispersion effect caused by heterogeneous electrode surface [16]. The impedance of CPE (Z_{CPE}) can be expressed as follows [38]:

$$Z_{\text{CPE}} = \frac{1}{Y_0(j\omega)^n} \quad (11)$$

where Y_0 denotes CPE constant; j denotes imagery root; ω denotes the angular frequency; and n denotes the phase shift index. Meanwhile, double layer capacitance (C_{dl}) can be also derived as per the following relationship [39]:

$$C_{\text{dl}} = (Y_0 R_{\text{ct}}^{1-n})^{1/n} \quad (12)$$

where Y_0 , R_{ct} and n have the same meanings as the abovementioned definitions. All impedance parameters are listed in Table 4. For steel specimen in the HDT-inhibited solution, R_{ct} increases from 10.97 $\Omega \cdot \text{cm}^2$ without inhibitor to 93.68 $\Omega \cdot \text{cm}^2$ with 1 mM HDT, and the optimal IE_z achieves as 88.29%. In contrast, R_{ct} value for ALT-protected specimen largely increases to 178.66 $\Omega \cdot \text{cm}^2$ with 1 mM dosage, from which the maximum IE_z reaches up to 93.86%. The corrosion inhibition effects of HDT and ALT can be fully attributed to their effective adsorption on steel surface, which also deservedly influence the

double layer at steel/solution interface. Accordingly, C_{dl} in Table 4 monotonously decrease with the augment of inhibitor concentration that agrees well with the following equation [40]:

$$C_{dl} = \frac{\varepsilon^0 \varepsilon^i}{d} \cdot S \quad (13)$$

where d denotes the thickness of double layer; S denotes the effective area of electrode; ε^0 and ε^i denote the air and local dielectric constants, respectively. The substitution of pre-adsorbed water molecules by organic species along the outer Helmholtz plane would increase the thickness of double layer and decrease in local dielectric constant [9]. Consequently, a downward trend of C_{dl} is observed with the increasing concentration of HDT and ALT. The inhibitor-covered steel surface is smoother than the corroded control, yielding a higher n value. The enhanced increment of R_{ct} and n , together with the significant decrease in C_{dl} , collectively points out that ALT is more efficient for the inhibition of steel corrosion in HCl solution than HDT. Overall, electrochemical outcomes agree well with the results of gravimetric measurements.

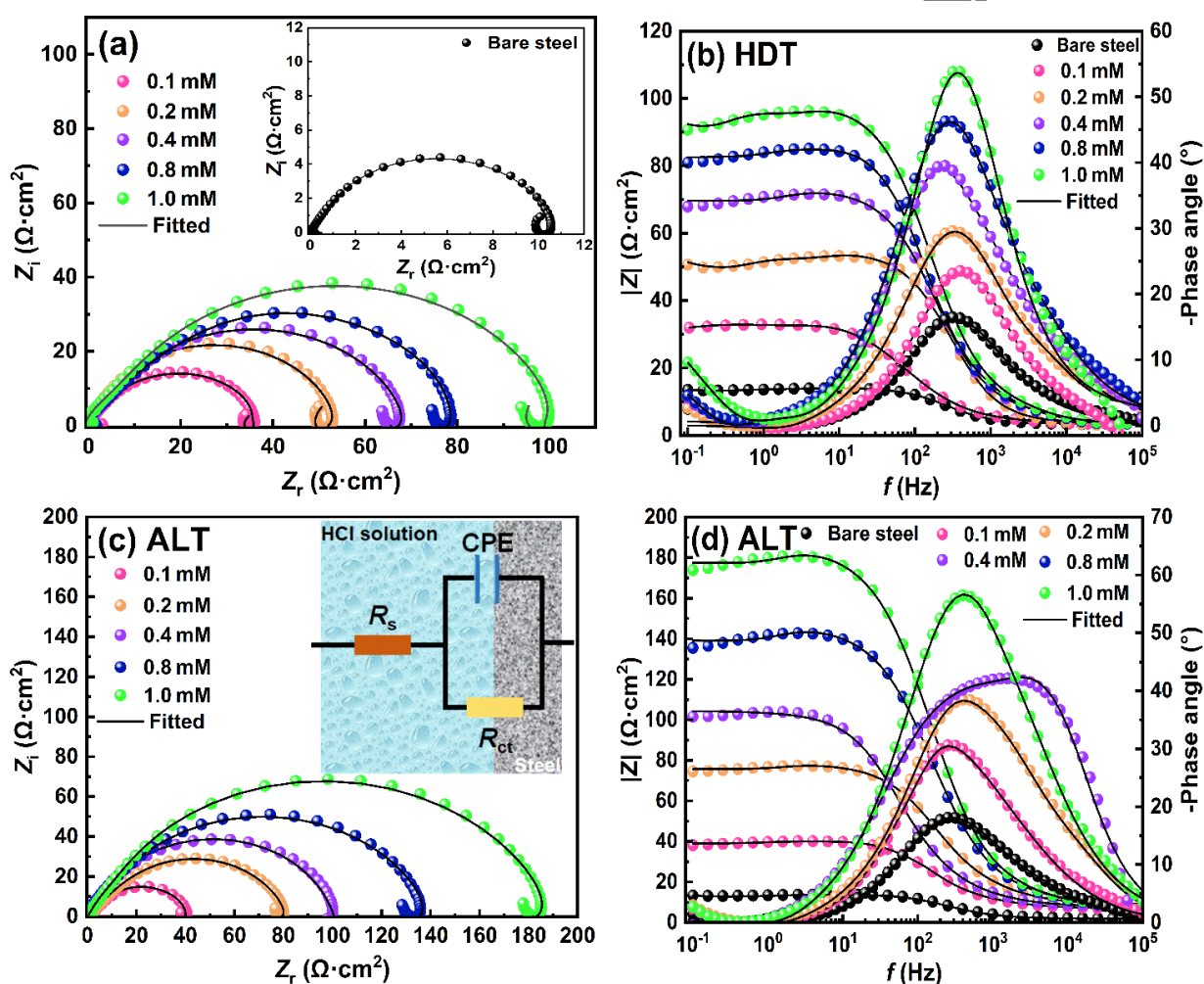


Figure 6. Nyquist (a, c) and Bode (b, d) spectra for 20# steel in 1 M HCl solution without (inset of a) and with different concentrations of HDT (upper) or ALT (lower) along with the equivalent circuit (inset of c)

Table 4. Impedance parameters for 20# steel in 1 M HCl solution without and with different concentrations of HDT and ALT at 303 K

Species	Concentration (mM)	R_{ct} ($\Omega \cdot \text{cm}^2$)	C_{dl} ($\mu\text{F}/\text{cm}^2$)	n	IE_z (%)
Blank	0	10.97	288.09	0.73	/
HDT	0.1	32.79	117.34	0.79	66.54
	0.2	50.25	85.21	0.85	78.17
	0.4	67.88	70.16	0.87	83.84
	0.8	82.54	55.20	0.87	86.71
	1.0	93.68	43.87	0.89	88.29
ALT	0.1	37.12	96.55	0.81	70.45
	0.2	76.87	75.49	0.83	85.73
	0.4	99.46	53.87	0.81	88.97
	0.8	139.21	32.90	0.89	92.12
	1.0	178.66	28.82	0.91	93.86

3.4 Theoretical modelling

3.4.1 Electronic scale simulation

Considering the structural difference between the studied inhibitors, the improvement of anticorrosive capacity for ALT depends largely on the grafted acid diamide group. Thus, theoretical calculations were performed to deeply decipher the enhanced anticorrosion mechanism and provide solid theoretical support for experimental observations.

Prior to electronic and atomic scale simulations, the microspecies analyses should be preferentially conducted on HDT and ALT to clarify their specific states in the corrosive medium. Figure 7a and b presents the species distribution of HDT and ALT in the aqueous solution with different pH values. Explicitly, both compounds keep the neutral state in 1 M HCl solution, which are used for the subsequent calculations for reactive descriptors including optimized structure, HOMO, LUMO and ESP. Figure 7c illustrates the reactive descriptors of HDT in the dominant solvent model. Obviously, HOMO and LUMO spread over the whole backbone of HDT. As is known, HOMO reflects the electron-donating ability of a molecule toward the metal substrate; while, LUMO indicates the active region for the molecule accepting free electrons escaped from metal surface [16]. In addition, ESP distribution on HDT features that the negative potential mainly concentrates on O heteroatoms; and these sites may be attracted by the positively charged steel surface in HCl solution. Figure 7d depicts the reactive descriptors of ALT in the dominant solvent model. HOMO propagates along the whole backbone of ALT, suggesting its strong electron donation capacity. While, LUMO primarily locates on the hydantoin ring, accommodating free electrons in the ambient environment. Owing to the throughout electro-donating effect, ALT emerges more significant negative surface potential as given in Figure 7d than HDT.

From density of state (DOS) analyses shown in Figure 7e and f, energy gaps (ΔE) of HDT and ALT can be obtained according to the expression:

$$\Delta E = E_L - E_H \quad (14)$$

where E_L and E_H denote the energies of LUMO and HOMO, respectively. Clearly, approximately equal values of ΔE are observed between HDT and ALT, i.e., 2.309 and 2.318 eV, respectively. This indicates that the similar potential barriers for an elementary charge on HDT and ALT to be conquered in the electron transfer reaction (e.g., chemisorption) [41]. Comprehensively analyzing the reactive descriptors of two compounds points out that ALT earns the superior electron-donating ability with intensified negative potential as compared to HDT. By comparing their molecular architecture, the grafted acid diamide group should be responsible for the divergent electronic structures. On that account, differential charge densities of HDT and ALT are projected on the molecular backbone as illustrated in the insets of Figure 7e and f, respectively. For HDT, O heteroatoms are centers for electron injection, which can donate the unpaired electrons to empty d-orbital of Fe atoms on steel surface. Another aspect, the presence of extra acid diamide group endows the fortified electron enrichment throughout ALT backbone besides further enhanced electron density on hydantoin ring. Moreover, additional inspection on Figure 7f finds that DOS of ALT in the vicinity of Fermi level (0 eV position) is more continuous with higher intensity than that of HDT. This reveals the strong electron transfer capability of ALT toward steel surface in the corrosive medium [39].

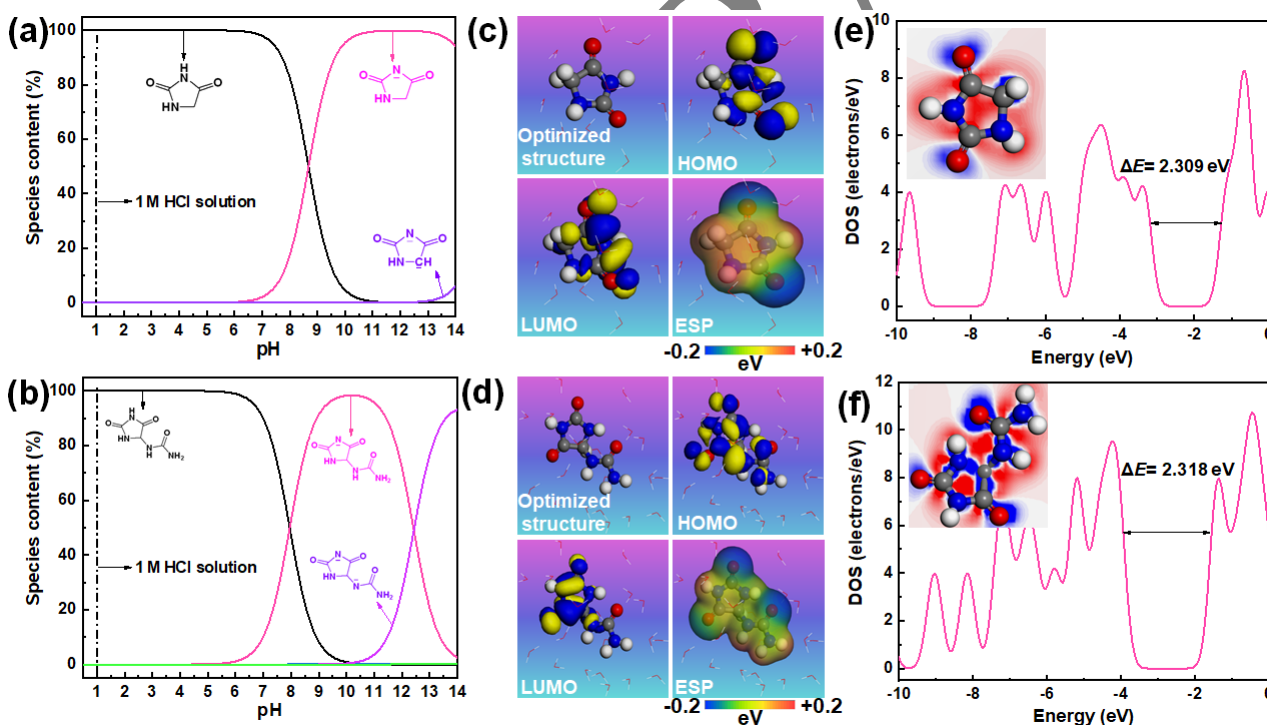


Figure 7. Species analysis (a, b), global reactive descriptors (c, d) and density of state plots (e, f; inset: difference charge density; blue: electrons accumulation; and red: electrons consumption) for HDT (upper) and ALT (lower)

3.4.2 Atomic scale simulation

MD simulation provides the direct view for the adsorption of inhibitor on metal surface [42]. Figure 8 presents the equilibrium snapshots of HDT and ALT adsorbed on Fe (100) plane in the designed

HCl solution at 303 K. It is observed from the vertical view that HDT (Figure 8a) and ALT (Figure 8b) adsorb on Fe (100) surface in a stretching mode. By this manner, heteroatoms (e.g., O and N) can further involve in the interaction with steel surface. Moreover, from the lateral view given in Figure 8a and b, parallel configuration is found for HDT on Fe (100) plane; while, ALT exhibits an imperfect parallel configuration with the acid diamide group oriented toward the bulk solution. Therefore, it is rational to assume that acid diamide group on ALT mainly behaves as a mediator for the electron distribution on hydantoin ring, which is the interacting center for the adsorption on steel surface. The fortified adsorption capacity of ALT can be also identified by its E_{inter} value on Fe (100) plane. The E_{inter} values for HDT and ALT deposited on metal surface was calculated as -465.86 and -729.31 kJ/mol, respectively. The negative sign of E_{inter} reveals that the adsorption of HDT and ALT on Fe (100) surface is energetically favorable [43]. In addition, larger magnitude of E_{inter} for ALT than that for HDT consolidates the resulting better corrosion inhibition effect.

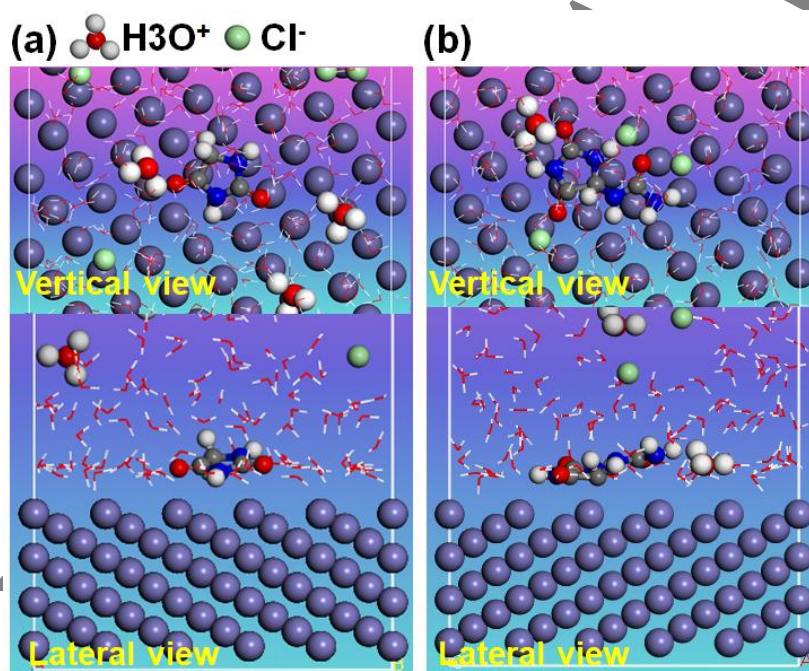


Figure 8. Vertical and lateral snapshots for HDT (a) and ALT (b) adsorbed on Fe (100) plane at 303 K

4. CONCLUSION

(1) HDT and ALT could efficiently inhibit the corrosion of 20# steel in 1 M HCl solution at 303 K, which exhibited the maximum IE_w value of 89.13% and 96.12%, respectively. Increasing temperature negatively affected the anticorrosive effect of both compounds.

(2) The anticorrosive efficacy of HDT and ALT resulted from their spontaneous adsorption on steel surface, which obeyed Langmuir isotherm. The corrosion activation energies were elevated by the augment of inhibitor concentration, indicating the enhanced barrier for the steel dissolution in HCl

medium. Negative sign of activation entropy revealed the ordered assembly of HDT and ALT at the steel/electrolyte interface.

(3) Due to the effective adsorption of HDT and ALT, i_{corr} value monotonously decreased; accordingly, the interfacial R_{ct} continuously augmented as the inhibitor dosage increased. The presence of HDT and ALT hardly affected the corrosion mechanism of steel in HCl solution, which could be regarded as the mixed-type corrosion inhibitors with dominantly anodic effect.

(4) The grafted acid diamide group could intensify the electron density around hydantoin ring, which acted as the adsorption center on steel surface. By virtue of the electron-donating effect, ALT was firmly anchored on steel surface with higher E_{inter} value than HDT, and thus exerted the better corrosion inhibition efficiency.

ACKNOWLEDGEMENT

Final support from Beijing Municipal Natural Science Foundation (2192016), National Natural Science Foundation of China (21606005), Support Project of High-level Teachers in Beijing Municipal Universities in the Period of 13th Five-year Plan (CIT&TCD201904042) and Opening Project of Material Corrosion and Protection Key Laboratory of Sichuan Province (2021CL20) are acknowledged.

Reference

1. X. G. Li, D. W. Zhang, Z. Y. Liu, Z. Li, C. W. Du and C. F. Dong, *Nature*, 527 (2015) 441-442.
2. H. Liu, B. M. Fan, Z. Y. Liu, X. Q. Zhao, B. Yang, X. W. Zheng and H. Hao, *J. Ind. Eng. Chem.*, (2021) <https://doi.org/10.1016/j.jiec.2021.11.004>
3. K. Kousar, M. S. Walczak, T. Ljungdahl, A. Wetzel, H. Oskarsson, P. Restuccia, E. A. Ahmad, N. M. Harrison and R. Lindsay, *Corros. Sci.*, 180 (2021) 109195.
4. E. Zaki, M. Abd-El-Raouf, A. Elaraby and T. Zidan, *Int. J. Electrochem. Sci.*, 16 (2021) 210374.
5. A. Dehghani, G. Bahlakeh and B. Ramezanzadeh, *Compos. Part. B-Eng.*, 197 (2020) 108152.
6. D. S. Chauhan, K. E. Mouaden, M. A. Quraishi and L. Bazzi, *Int. J. Biol. Macromol.*, 152 (2020) 234-241.
7. W. W. Zhang, B. L. Nie, H. J. Li, Q. Y. Li, C. Y. Li and Y. C. Wu, *Carbohydr. Polym.*, 260 (2021) 117842.
8. N. Rajamohan, F. S. Z. S. Al Shibli and M. Rajasimman, *Environ. Res.*, 203 (2021) 111816.
9. H. Liu, B. M. Fan, G. F. Fan, X. Q. Zhao, Z. N. Liu, H. Hao and B. Yang, *J. Alloy. Compd.*, 872 (2021) 159752.
10. Y. L. Kobzar and K. Fatyeyeva, *Chem. Eng. J.*, 425 (2021) 131480.
11. G. F. Fan, H. Liu, B. M. Fan, Y. C. Ma, H. Hao and B. Yang, *J. Mol. Liq.*, 311 (2020) 113302.
12. D. J. Li, X. Q. Zhao, Z. N. Liu, H. Liu, B. M. Fan, B. Yang, X. W. Zheng, W. Z. Li and H. J. Zou, *ACS Omega*, 6 (2021) 29965-29981.
13. S. Z. Salleh, A. H. Yusoff, S. K. Zakaria, M. A. A. Taib, A. Abu Seman, M. N. Masri, M. Mohamad, S. Mamat, S. A. Sobri, A. Ali and P. T. Teo, *J. Clean. Prod.*, 304 (2021) 127030.
14. M. E. Khalifa, I. H. El Azab, A. A. Gobouri, G. A. M. Mersal, S. Alharthi, M. Saracoglu, F. Kandemirli, J. Ryl and M. A. Amin, *J. Colloid. Interf. Sci.*, 580 (2020) 108-125.
15. A. Saady, Z. Rais, F. Benhiba, R. Salim, K. Ismaily Alaoui, N. Arrousse, F. Elhadjaji, M. Taleb, K. Jarmoni, Y. Kandri Rodi, I. Warad and A. Zarrouk, *Corros. Sci.*, 189 (2021) 109621.
16. L. O. Olasunkanmi and E. E. Ebenso, *J. Colloid. Interf. Sci.*, 561 (2020) 104-116.
17. G. A. Gaber, S. Hosny and L. Z. Mohamed, *Int. J. Electrochem. Sci.*, 16 (2021) 211214.
18. L. Huang, K. P. Yang, Q. Zhao, H. J. Li, J. Y. Wang and Y. C. Wu, *Bioelectrochemistry*, 143 (2022) 107969.

19. T. W. Quadri, L. O. Olasunkanmi, O. E. Fayemi, E. D. Akpan, C. Verma, E.-S. M. Sherif, K. F. Khaled and E. E. Ebenso, *Coordin. Chem. Rev.*, 446 (2021) 214101.
20. Y. J. Qiang, L. Guo, H. Li and X. J. Lan, *Chem. Eng. J.*, 406 (2021) 126863.
21. Y. C. Ma, B. M. Fan, M. M. Wang, B. Yang, H. Hao, H. Sun and H. J. Zhang, *Chem. J. Chin. Univ.*, 40 (2019) 1706-1716.
22. B. M. Fan, H. Hao, B. Yang and Y. Li, *Res. Chem. Intermediat.*, 44 (2018) 5711-5736.
23. A. Farhadian, A. Rahimi, N. Safaei, A. Shaabani, E. Sadeh, M. Abdouss and A. Alavi, *ACS Appl. Mater. Inter.*, 13 (2021) 3119-3138.
24. Y. C. Ma, B. M. Fan, H. Hao, J. Y. Lu, Y. H. Feng and B. Yang, *Chem. J. Chin. Univ.*, 40 (2019) 96-107.
25. A. S. Al-Gorair, H. Hawsawi, A. Fawzy, M. Sobhi, A. Alharbi, R. S. A. Hameed, S. Abd El Wanees and M. Abdallah, *Int. J. Electrochem. Sci.*, 16 (2021) 211119.
26. B. M. Fan, Y. C. Ma, M. M. Wang, H. Hao, B. Yang, J. Y. Lv and H. Sun, *J. Mol. Liq.*, 292 (2019) 111446.
27. R. Natarajan and F. S. Z. S. Al Shibli, *Chemosphere*, 284 (2021) 131375.
28. H. Lgaz, S. K. Saha, A. Chaouiki, K. S. Bhat, R. Salghi, Shubhalaxmi, P. Banerjee, I. H. Ali, M. I. Khan and I.-M. Chung, *Constr. Build. Mater.*, 233 (2020) 117320.
29. J. Haque, V. Srivastava, M. A. Quraishi, D. Singh Chauhan, H. Lgaz and I.-M. Chung, *Corros. Sci.*, 172 (2020) 108665.
30. S. G. Meng, Z. N. Liu, X. Q. Zhao, B. M. Fan, H. Liu, M. Guo and H. Hao, *RSC Adv.*, 11 (2021) 31693-31711.
31. B. M. Fan, H. Hao, A. R. Guo and R. P. Yang, *J. Water Reuse Desal.*, 6 (2016) 399-412.
32. B. M. Fan, G. Wei, H. Hao, A. R. Guo and J. Li, *Desalin. Water Treat.*, 57 (2016) 17308-17321.
33. J. Halambek, I. Cindric and A. Nincevic Grassino, *Carbohydr. Polym.*, 234 (2020) 115940.
34. Y. C. Ma, B. M. Fan, T. T. Zhou, H. Hao, B. Yang and H. Sun, *Polymers*, 11 (2019) 635.
35. Y. C. Ma, B. M. Fan, H. Liu, G. F. Fan, H. Hao and B. Yang, *Appl. Surf. Sci.*, 514 (2020) 146086.
36. L. Guo, J. H. Tan, S. Kaya, S. L. Leng, Q. B. Li and F. Zhang, *J. Colloid Interf. Sci.*, 570 (2020) 116-124.
37. L. Guo, R. L. Zhang, B. C. Fan, W. P. Li, H. Y. Liu and S. Z. Wu, *J. Mol. Liq.*, 310 (2020) 113239.
38. B. M. Fan, Z. N. Liu, X. Q. Zhao, H. Liu, G. F. Fan and H. Hao, *Colloid. Surface. A*, 629 (2021) 127434.
39. A. H. Tantawy, K. A. Soliman and H. M. Abd El-Lateef, *J. Clean. Prod.*, 250 (2020) 119510
40. H. Liu, B. M. Fan, G. F. Fan, Y. C. Ma, H. Hao and W. Zhang, *J. Mater. Sci. Technol.*, 72 (2021) 202-216.
41. Y. C. Ma, T. T. Zhou, W. Q. Zhu, B. M. Fan, H. Liu, G. F. Fan, H. Hao, H. Sun and B. Yang, *J. Mol. Model.*, 26 (2020) 81.
42. M. M. Wang, B. M. Fan, B. Y. Wen and C. Jiang, *Sci. China Technol. Sc.*, 63 (2020) 2098-2112.
43. H. Li, Y. J. Qiang, W. J. Zhao and S. T. Zhang, *Corros. Sci.*, 191 (2021) 109715.